

# Molecular Doped Biodegradable Triboelectric Nanogenerator with Optimal Output Performance

Cong Li, Ruizeng Luo, Yuan Bai, Jiajia Shao, Jianying Ji, Engui Wang, Zhe Li, Hongyu Meng,\* and Zhou Li\*

Biodegradable polymers (BPs)-based triboelectric nanogenerators (TENGs) have advantages, including biocompatibility and biodegradability. However, biodegradable TENGs (BD-TENGs) possess relatively low output performance, limiting their application due to the small differences in triboelectric polarities for most BPs. Molecular doping is a simple and effective method in altering the triboelectric polarity of triboelectric materials and improving the output performance of BD-TENGs. However, there is a lack of laws and mechanism about the differences in triboelectric polarities of different doped molecules, especially of molecules with biodegradability and biocompatibility. Here, kinds of doping molecules are selected for doping in tribopositive and tribonegative materials, respectively, and their triboelectric polarities and related laws are researched. In particular, the output performance of BD-TENG is improved several times by doping small amounts of poly (propylene glycol) (PPG) and ethyl cellulose (EC), with enhanced resolution in abnormal respiratory signal monitoring. This work not only provides theoretical guidance for the selection of triboelectric molecules but also conducts in-depth research in molecular-level triboelectric mechanisms.

## 1. Introduction

Triboelectric nanogenerators (TENGs) can convert irregular mechanical energy into electricity based on the coupling effects of triboelectrification and electrostatic induction, serving broad applications in energy harvesting and sensing.<sup>[1]</sup> Specifically, biodegradable triboelectric nanogenerators (BD-TENGs) exhibit characteristics such as biocompatibility, biodegradability, or environmental friendliness because they can be degraded in the natural environment or absorbed or metabolized by the human body.<sup>[2]</sup> Biodegradable triboelectric polymers (BTPs) are the foundational materials for the fabrication of triboelectric layers in BD-TENGs.<sup>[3]</sup> Compared with some common non-BTPs (such as nylon and PTFE)<sup>[4]</sup> with the large difference in triboelectric polarities, different kinds of BTPs (including polysaccharides, proteins, or polyesters, et al.) exhibit similar and tribopositive

polarities due to their functional groups tend to have electron-donating (ED) ability.<sup>[5]</sup> The similarity in triboelectric polarity leads to the limited performances in the electrical output of BD-TENGs based on BTPs.

Enhancing the output performance of BD-TENGs is crucial for breaking through their application barriers. Methods to improve the output performance encompass the selection, surface modification, or doping of triboelectric materials, structure optimization, and electrode optimization.<sup>[6]</sup> Among them, molecular doping of triboelectric materials is a simple and practical approach to improve the output performance. The mechanism of molecular doping is introducing molecules with greater triboelectric polarities into tribopositive and tribonegative layers, respectively, to increase their triboelectric polarities difference. There are some reports about molecular doping of BD-TENGs,<sup>[6c,7]</sup> but few studies compare the difference in triboelectric polarity of various doped molecules and explain related mechanisms, especially regarding biocompatible or biodegradable molecules.

Here, we selected eight biocompatible doping molecules for tribopositive and tribonegative materials, respectively, considering their biocompatibility, biodegradability, chemical group or element characteristics, and triboelectric polarity. The changes in triboelectric polarity after doping and related mechanisms were studied in depth. In particular, the open circuit voltage ( $V_{oc}$ ), short circuit current ( $I_{sc}$ ), and transfer charge ( $Q_{sc}$ ) of the doped

C. Li  
School of Chemistry and Chemical Engineering  
Guangxi University  
Nanning, Guangxi 530004, China

C. Li, R. Luo, Y. Bai, J. Shao, J. Ji, E. Wang, Z. Li, H. Meng, Z. Li  
Beijing Institute of Nanoenergy and Nanosystems  
Chinese Academy of Sciences  
Beijing 101400, China  
E-mail: [menghongyu@iccas.ac.cn](mailto:menghongyu@iccas.ac.cn); [zli@binn.cas.cn](mailto:zli@binn.cas.cn)

R. Luo, J. Shao, E. Wang, Z. Li  
School of Nanoscience and Engineering  
University of Chinese Academy of Sciences  
Beijing 100049, China

Y. Bai, J. Ji, Z. Li  
Center on Nanoenergy Research  
School of Physical Science and Technology  
Guangxi University  
Nanning, Guangxi 530004, China

Z. Li  
Department of Neurology  
Aerospace Center Hospital  
School of Life Science  
Beijing Institute of Technology  
Beijing 100081, China

 The ORCID identification number(s) for the author(s) of this article can be found under <https://doi.org/10.1002/adfm.202400277>

DOI: 10.1002/adfm.202400277

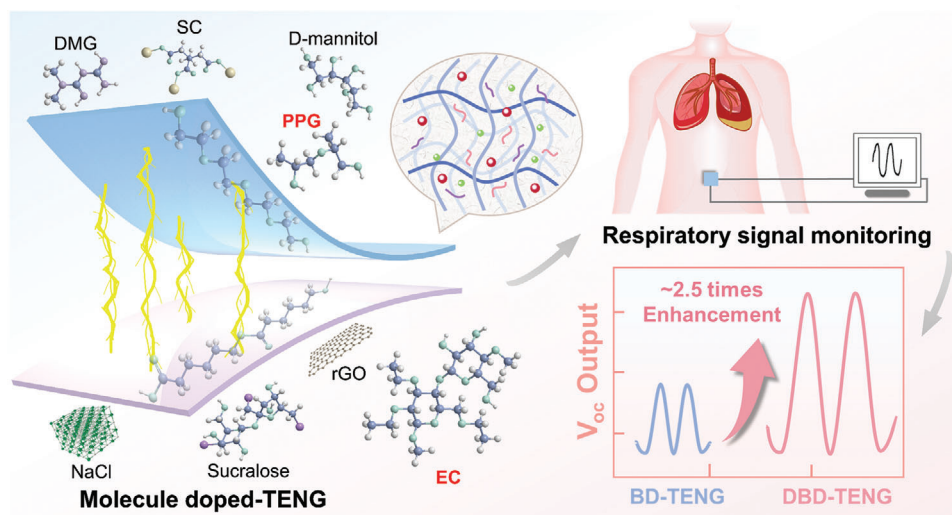


**Figure 1.** Schematic illustration of DBD-TENG and its application in respiratory signal monitoring.

BD-TENG (DBD-TENG) were enhanced by 2.73, 2.60, and 2.44 times, respectively, after doping small amounts of poly(propylene glycol) (PPG) and ethyl cellulose (EC) with low molecular weight into tribopositive and tribonegative biodegradable polymers (BPs). The DBD-TENG showed a significant improvement in the resolution of abnormal respiratory signal monitoring (Figure 1 and Figure 6). This work not only provides theoretical guidance for the selection of biocompatible triboelectric molecules but also conducts in-depth research in molecular-level triboelectric mechanisms.

## 2. Results and Discussion

### 2.1. The Selection of BTPs

We selected four types of BPs with good flexibility, mechanical properties, and biodegradability as candidate BTPs before doping, including polyethylene oxide (PEO), hydroxypropyl cellulose (HPC), polylactic acid (PLA), and polycaprolactone (PCL) (Figure 2a; Figures S1 and S2, Supporting Information), and then sorted their triboelectric polarities. These four BTPs significantly differ in the types of main- or side-chain chemical groups or group density. Therefore, they are expected to possess obvious distinctions in triboelectric polarity when used as triboelectric layers of BD-TENG. According to the triboelectric performance based on the comparison of  $V_{oc}$ ,  $I_{sc}$ , and  $Q_{sc}$ , the order of four BTPs in triboelectric polarities (from positive to negative) is PEO (20.24 nC), HPC (19.32 nC), PLA (15.05 nC), and PCL (12.73 nC) (Figure 2b–d). For PEO, because of the repeating oxyethylene group ( $[-CH_2CH_2O-]_n$ ) with strong ED ability on the main chain, PEO is considered to possess strong positive polarity, even higher than common tribopositive polymer polyamide.<sup>[6a]</sup> The PEO film was tested to have the highest positive polarity in this work. HPC is the cellulose derivative with hydroxypropylated side chains. Its main chain contains abundant repeating glycosidic bonds, which have a similar structure and triboelectric polarity as the ( $[-CH_2CH_2O-]_n$ ) in PEO, but more alkane proportions in its repeating units. In addition, its plenti-

ful  $[-CH_2CH(CH_3)O-]_n$  side-chain groups also show prominent positive polarity. The test results show that the triboelectric positive polarity of HPC is second only to PEO, which is attributed to the relatively high proportion of alkanes in its repeating units. PLA and PCL belong to poly ( $\alpha$ -esters) with abundant main-chain ester bonds. According to the results, the positive polarities of PLA and PCL are weaker than those of PEO and HPC containing repeating ether bonds.<sup>[8]</sup> In comparison, PLA has stronger positive polarity than PCL due to its higher ester group proportion but lower alkane proportion in the main chain of molecules.<sup>[9]</sup> We inferred that the strength of the triboelectric positive polarity or the ED ability of different groups follows the order ether group > ester group > alkane group. So, we selected PEO and PCL as the tribopositive and tribonegative layers of DBD-TENG for the following research.

### 2.2. The Selection and Properties of Doping Molecules

We select eight doping molecules with potential triboelectric positive polarity, including spermidine (SPD, with amine groups ( $-NH_2$ )), 1,1-Dimethylguanidine (DMG, with guanidino groups ( $-CN_3H_4$ )), citric acid (CA, with carboxyl groups ( $-COOH$ )), sodium citrate (SC, with carboxylate groups ( $-COO^-$ )), glycerol and D-mannitol (with hydroxyl groups ( $-OH$ )), and poly (ethylene glycol) (PEG) and PPG (with polyether groups) with low average molecular weight ( $M_w$ ) (Figure 3a). Most of the eight organic molecules are foods or food additives with biocompatibility and absorbability, and DMG, PEG, or PPG can be used as pharmaceutical or cosmetic ingredients. Their chemical groups have been reported to possess potential desirable positive polarity.<sup>[5,10]</sup> Compared with pure PEO film, the triboelectric positive polarities of the PEO/molecule composite films doping 10 wt% of the eight molecules (see FTIR spectra of Figure S3a,b, Supporting Information), respectively, are all enhanced. The surface morphology of most PEO/molecule composite films does not change significantly (SEM images of Figure S5, Supporting Information), except for PEO/DMG and PEO/CA films, which is speculated

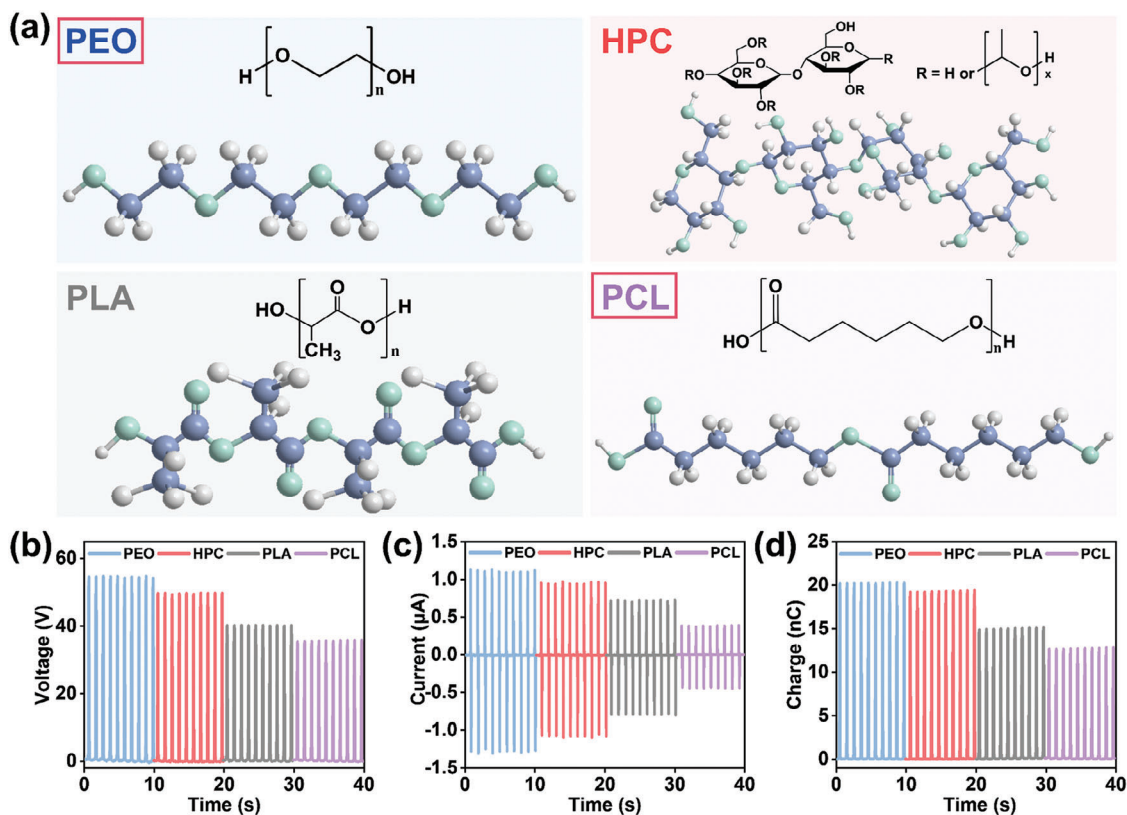


**Figure 2.** a) Molecular structure of four BPs, PEO, HPC, PLA, and PCL. The output results of four BTPs contacting with PTFE, including b)  $V_{oc}$ , c)  $I_{sc}$ , and d)  $Q_{sc}$ .

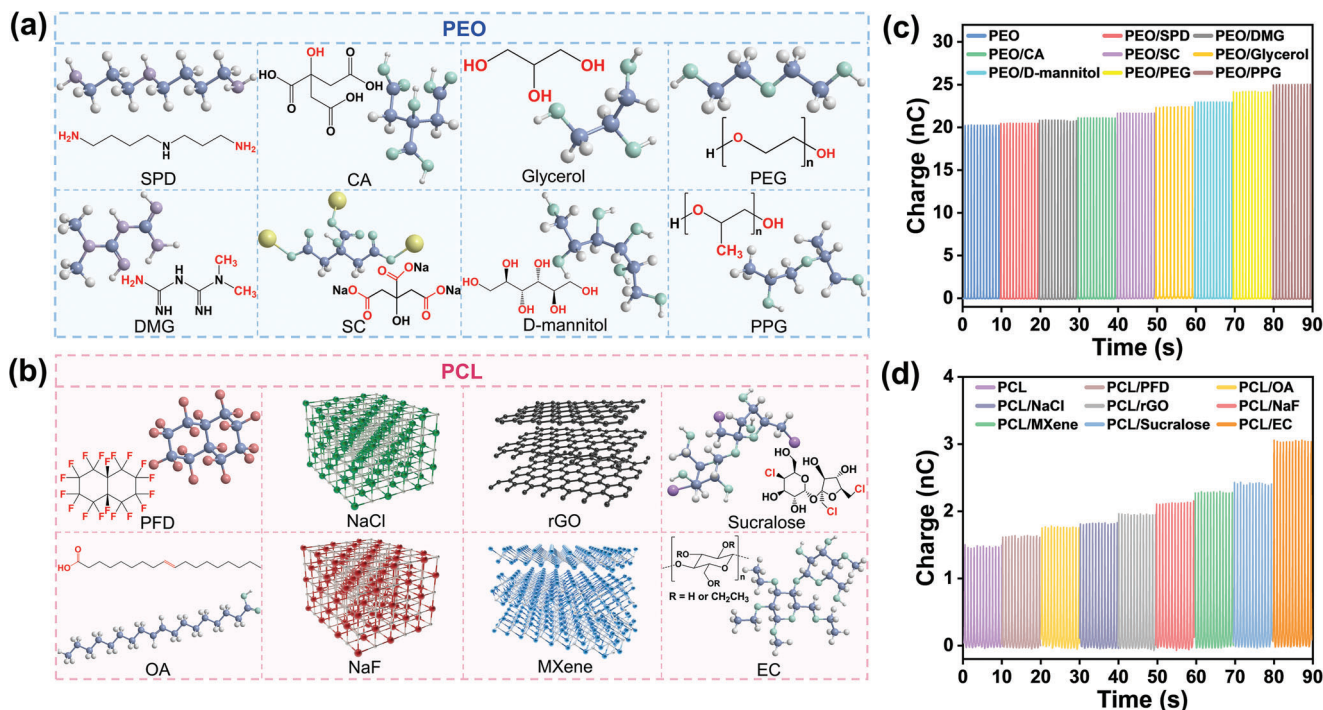


**Figure 3.** Molecular structure of doping molecules for a) PEO and b) PCL film. The ranking of the  $Q_{sc}$  of c) PEO/molecule and d) PCL/molecule composite films.

due to the relatively low solubility of DMG and CA in water. The introduction of doping molecules leads to varying degrees of increase or decrease in the maximum tensile stress of the PEO film, but all films maintain excellent integrity (Figure S4a, Supporting Information). According to the enhancement effect, we infer that the order of these doping molecules in ED ability (from strong to weak) is PPG, PEG, D-mannitol, glycerol, SC, CA, DMG, and SPD (Figure 3c). Polymers with polyether groups are demonstrated to possess more optimal ED and triboelectric positive abilities,<sup>[5]</sup> which also applies to PPG and PEG with lower molecular weight in this work. After doping, PEO/PPG and PEO/PEG composite films exhibit the most positive polarities among the eight PEO-based composite films. Compared with PEO/PEG film, PEO/PPG film shows higher positive polarity because the side-chain methyl groups ( $-\text{CH}_3$ ) of PPG tend to enhance the ED ability of the molecule.<sup>[11]</sup> PEO/D-mannitol and PEO/glycerol composite films also exhibit great triboelectric positive ability, second only to PEO/PPG and PEO/PEG, because D-mannitol and glycerol molecules possess abundant  $-\text{OH}$  groups with good ED ability.<sup>[12]</sup> The triboelectric positive polarities of PEO/SC, PEO/CA, PEO/DMG, and PEO/SPD composite films are improved to varying degrees compared with the pure PEO film, which is attributed to the good ED ability of  $-\text{COO}^-$ ,  $-\text{COOH}$ ,  $-\text{CN}_3\text{H}_4$  and  $-\text{NH}_2$  of these doping molecules. Wherein PEO/SC exhibits higher positive polarity than PEO/CA due to  $-\text{COO}^-$  of the SC molecule being relatively prone to losing electrons and becoming  $-\text{COOH}$ , showing stronger ED ability. PEO/DMG exhibits higher triboelectric positive polarity than PEO/SPD because the DMG molecule has a higher amino group ratio than the SPD molecule.<sup>[13]</sup> Moreover, although PEO/D-mannitol and PEO/glycerol films exhibit higher triboelectric positive polarity than PEO/SC, PEO/CA, PEO/DMG, and PEO/SPD, it cannot directly prove that  $-\text{OH}$  (in D-mannitol or glycerol molecules) has stronger ED ability than  $-\text{COO}^-$ ,  $-\text{COOH}$ , or  $-\text{NH}_2$ ,<sup>[5,13]</sup> because  $-\text{OH}$  has a higher proportion in D-mannitol or glycerol molecules. Consequently, we selected the PEO/PPG composite film, exhibiting the highest positive polarity, as the tribopositive material for DBD-TENG.

We also select eight doping molecules (Figure 3b) with potential triboelectric negative polarity, which include MXene ( $\text{Ti}_3\text{C}_2\text{T}_x$ , 2D material with F element), reduced graphene oxide (rGO, 2D material), sodium chloride (NaCl, with chloride ion ( $\text{Cl}^-$ )), sodium fluoride (NaF, with fluoride ion ( $\text{F}^-$ )), oleic acid (OA, with a long alkane chain), perfluorodecalin (PFD, with 18 fluorine atoms (F)), sucralose (with 3 chlorine atoms (Cl)), and EC with low molecular weight (with side-chain  $-\text{OCH}_2\text{CH}_2$  groups). These eight molecules exhibit good biocompatibility within a specific doping range. Specifically, 2D materials MXene and rGO have been researched in biomedical applications.<sup>[14]</sup> NaCl and NaF are inorganic salts. NaCl is the main component of physiological saline, and NaF is a micro additive in toothpaste that can promote enamel remineralization.<sup>[15]</sup> PFD is a non-toxic ingredient of artificial blood that the human body can excrete.<sup>[16]</sup> OA and sucralose are food ingredients, and EC is a non-toxic cellulose derivative. The negative polarities of PCL/molecule composite films are enhanced to varying degrees after doping 10 wt% of the above eight molecules in PCL (see FTIR spectra of Figure S3c, Supporting Information). Due to the poor solubility of three

doping molecules in 1,1,1,3,3,3-Hexafluoro-2-propanol, the bottom flatness of PCL/NaCl, PCL/NaF, and PCL/sucralose composite films is slightly affected, while the others exhibit no obvious changes according to SEM images in Figure S6 (Supporting Information). Additionally, compared with PCL, the maximum tensile stress of PCL/EC composite film is slightly increased, whereas other PCL/molecule composite films are decreased moderately (Figure S4b, Supporting Information). According to the results, the order of PCL/molecule composite films in electron-withdrawing (EW) ability (from strong to weak) is PCL/EC, PCL/sucralose, PCL/MXene, PCL/NaF, PCL/rGO, PCL/NaCl, PCL/OA, and PCL/PFD (Figure 3d). PCL/EC composite film exhibits the strongest negative polarity because each unit of EC contains more than one side-chain  $-\text{OCH}_2\text{CH}_3$ , and  $-\text{OCH}_2\text{CH}_3$  possesses a good EW inductive effect, significantly enhancing the triboelectric negative ability of the PCL layer.<sup>[5]</sup> The sucralose molecule contains three  $-\text{Cl}$  atoms, and  $-\text{Cl}$  atoms endow the sucralose molecule with high EW ability,<sup>[11]</sup> resulting in great negative polarity for PCL/sucralose composite film, second only to PCL/EC film. For 2D material MXene, some of the T atoms refer to F elements (EDS spectrum of Figure S6f, Supporting Information). With its electron-trapping ability of multi-layered 2D structures, PCL/MXene composite film obtains a significantly enhanced negative ability compared with pure PCL film.<sup>[17]</sup> Similarly, 2D material rGO also possesses the electron-trapping ability, leading to increased negative polarity of PCL/rGO composite film.<sup>[7b]</sup> In this work, the doping content of rGO in PCL is relatively low (1 wt%), resulting in a weaker negative polarity than that of PCL/MXene. With the further increased doping content of rGO, the negative polarity of PCL/rGO composite film is anticipated to improve further. However, the large quantity, due to its tiny density ( $<0.10 \text{ g cm}^{-3}$ ) of more rGO, caused the deterioration in the morphological integrity and mechanical performance of PCL/rGO film (Figure S7, Supporting Information). Therefore, we determined the doping content of rGO to be 1 wt%. Inorganic salts NaF and NaCl are reported to have high electron affinity,<sup>[18]</sup> which improves EW ability, resulting in more negative polarities for PCL/NaF or PCL/NaCl than pure PCL film. PCL/OA composite film also shows a certain enhancement in negative polarity because the long-chain alkane in the OA molecule has stronger EW abilities than groups in those negative doping molecules.<sup>[6c]</sup> In addition, unsaturated groups ( $-\text{CH}=\text{CH}-$ ) in OA also exhibit stronger electron affinity than saturated groups ( $-\text{CH}_2-\text{CH}_2-$ ).<sup>[11]</sup> Even so, the improvement in EW ability or negative polarity of OA on PCL composite film is weaker than that of electron capture agents, inorganic salts, or organics containing halogens. The PFD molecule contains 18 F atoms and can be well dispersed with PCL. Therefore, it is expected to significantly enhance the negative polarity of the PCL film when doped. However, most PFD was apt to evaporate during the film formation,<sup>[16]</sup> leaving little in the composite film, as shown in the EDS image (Figure S6a, Supporting Information), leading to PCL/PFD film achieving minimal improvement in ED ability and negative polarity. Therefore, we selected the PCL/EC composite film, which revealed maximum improvement in negative polarity, as the tribonegative material for DBD-TENG.

We tested the molecular doping content (PPG or EC) for the optimal triboelectric output performance (Figure 4a,b).

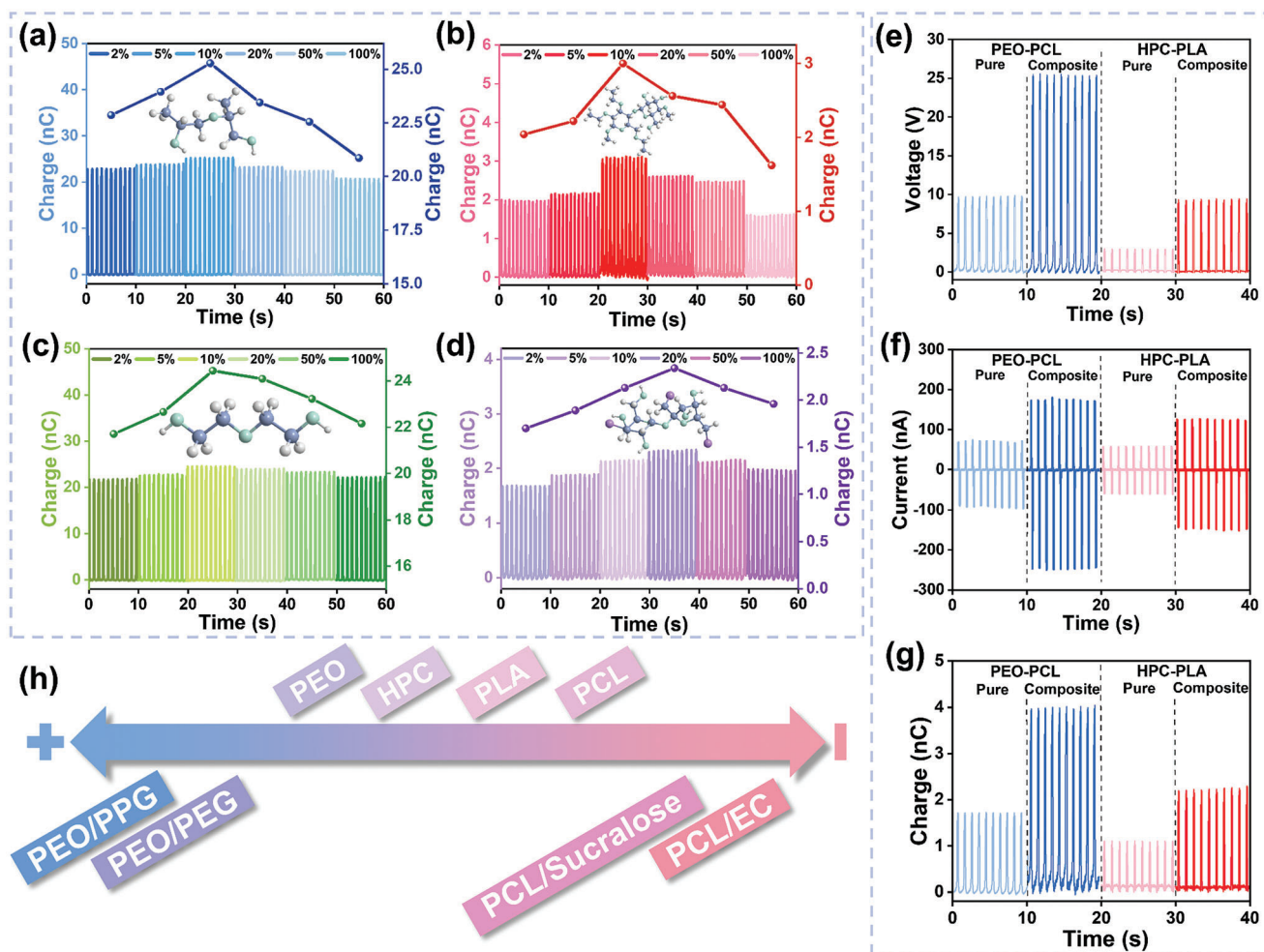


**Figure 4.** The influence of molecular doping content on the  $Q_{sc}$  of composite films, including a) PPG, b) EC, c) PEG, and d) sucralose. Triboelectric output results of PEO-PCL and HPC-PLA triboelectric pairs before and after doping on the first day, including e)  $V_{oc}$ , f)  $I_{sc}$ , and g)  $Q_{sc}$ . h) The triboelectric series of four BTPs and four composite films.

Compared with pure PEO or PCL film, the triboelectric polarity of composite films (FTIR spectra of Figure S8, Supporting Information) improves within the range of 2–100 wt% doping content. When the doping content in PEO/PPG or PCL/EC composite film reaches 10 wt%, composite films obtain the maximum output results without obvious influence on their mechanical properties (Figure S9, Supporting Information). When the doping content is less than 10 wt%, the tested  $Q_{sc}$  of composite films gradually increases as the triboelectric polarity enhances. Theoretically, the triboelectric polarity (or  $Q_{sc}$ ) of composite films will be further improved as the doping content increases. However, the surface flatness of composite films is seriously damaged due to the phase separation of two different molecules when the doping content reaches more than 10 wt% (SEM images of Figure S10, Supporting Information). This reduces the actual contact area between triboelectric layers and the charge transfer efficiency during contact separation, thus causing  $Q_{sc}$  to decrease.<sup>[19]</sup> Moreover, the phase separation of the doping molecule and polymer matrix generates gaps in the interfaces of composite films during the dynamic operation. The high resistance caused by the

gaps affects the electrical transmission of composite films, resulting in lower triboelectric output.<sup>[20]</sup> The same rule also applies to other doping molecules, such as PEG and sucralose (Figure 4c,d). Based on the results, PEO/PPG and PCL/EC composite films with 10 wt% doping content were chosen as tribopositive and tribonegative materials for DBD-TENG. The  $V_{oc}$ ,  $I_{sc}$ , and  $Q_{sc}$  of the PEO-PCL pair are enhanced by 2.73, 2.60, and 2.44 times to 25.13 V, 252.10 nA, and 4.10 nC respectively after doping. 10 wt% PPG and 10 wt% EC were also doped into HPC and PLA, respectively, to prove that the output performance improvement brought about by doping applies to more polymer matrixes. The HPC-PLA pair modified by molecular doping generates a 3.24, 2.60, and 1.96-times enhancement on the  $V_{oc}$ ,  $I_{sc}$ , and  $Q_{sc}$  to 9.23 V, 154.60 nA, and 2.17 nC, respectively. The triboelectric output results for five consecutive days (Figure S11, Tables S2 and S3, Supporting Information) exhibit that molecular doping enables a stable improved output, and the output signals measured on the first day are shown in Figure 4e–g. The positions of four composite films in the triboelectric series are illustrated in Figure 4h.

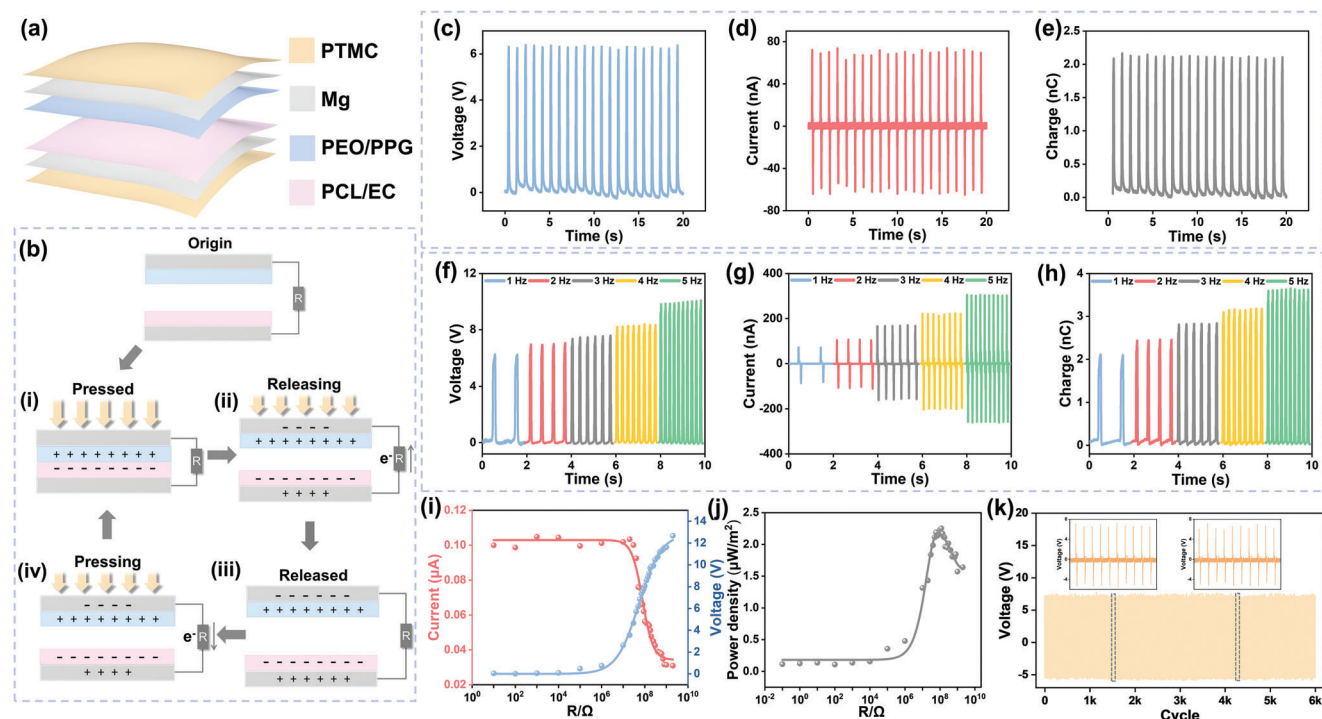


**Figure 5.** Structural design, working principle, and output performance of DBD-TENG. a) Schematic illustration of DBD-TENG. b) The working mechanism of DBD-TENG in a complete CS cycle, including i) fully contact, ii) gradually separated, iii) fully released, and iv) gradually approaching. The output results of DBD-TENG, including c)  $V_{oc}$ , d)  $I_{sc}$ , and e)  $Q_{sc}$ . Frequency-response characteristics of DBD-TENG under loading frequencies from 1 to 5 Hz, including f)  $V_{oc}$ , g)  $I_{sc}$ , and h)  $Q_{sc}$ . The variation of i) peak voltage, peak current, and j) peak power density of DBD-TENG with different external load resistance. k) The stability test of DBD-TENG under continuous operation for 6000 cycles.

### 2.3. Preparation and Output Characterization of DBD-TENG

The as-prepared DBD-TENG has a multi-layered structure: poly (trimethylene carbonate) (PTMC) encapsulation layer, magnesium (Mg) electrode, PEO/PPG tribopositive layer, and PCL/EC tribonegative layer (Figure 5a), with a device size of 2.5 cm × 2.5 cm × 1.45 mm (Figure S12a,b, Supporting Information). The device is highly flexible and can be bent arbitrarily (see Figure S12c, Supporting Information). The working mechanism of DBD-TENG is schematically illustrated in Figure 5b, which operates in vertical contact-separation (CS) mode. At the original state, as PEO/PPG is far from PCL/EC, both triboelectric layers are charge-balanced without generating output signals. i) As an external force is applied on DBD-TENG, the triboelectric layer surfaces contact and rub with each other, making PEO/PPG positively charged and PCL/EC negatively charged because of their different triboelectric polarities. ii) Subsequently, when PEO/PPG is gradually separated from PCL/EC, a potential difference is generated between two triboelectric layers to drive the flow of electrons in the external circuit until iii) reaches an equilibrium when two triboelectric layers are fully released. iv) As an external force is applied to the device again, the electrons flow reversely to reach a new equilibrium. Therefore, alternating current is generated during periodic contact and separation.

The output performance of DBD-TENG was characterized (Figure 5c–e), obtaining a  $V_{oc}$  of 6.30 V, an  $I_{sc}$  of 72.05 nA, and a  $Q_{sc}$  of 2.12 nC. The dependence of the device output on the vibration frequency is shown in Figure 5f–h. Under the low-frequency

range (1–5 Hz), the  $V_{oc}$  increases from 6.28 to 10.10 V,  $I_{sc}$  from 72.05 to 302.66 nA, and  $Q_{sc}$  from 2.12 to 3.63 nC. Different resistances will affect the peak voltage and current of DBD-TENG (Figure 5i). As load resistance increases to several mega ohms, the peak current decreases while the peak voltage rises rapidly. When the load resistance reaches several thousand mega ohms, the peak current reduces to a relatively stable state. The maximum peak power density of 2.25  $\mu\text{W m}^{-2}$  is obtained at  $\approx 120 \text{ M}\Omega$  (Figure 5j). After 6000 cycles of contact separation, the voltage output of the device remains stable at  $\approx 6.30 \text{ V}$  (100% of the initial value) (Figure 5k), demonstrating excellent stability.

### 2.4. Respiratory Monitoring and Sensing

Respiratory characteristics (including respiratory rate and depth) are vital for assessing human physical state.<sup>[21]</sup> The as-prepared DBD-TENG is a flexible transient wearable respiratory sensor to monitor breath signals. Sensitivity is a paramount parameter in sensor performance, denoting the sensor's responsiveness to tiny variations in the parameter under examination (the respiratory signals in this study), which is reflected in differences within the output signals.<sup>[22]</sup> The DBD-TENG and PEO@PCL-TENG were fixed on the volunteer's abdomen, yielding oscillatory signals (Figure 6a). A complete breathing cycle encompasses inhalation and exhalation phases.<sup>[23]</sup> Due to the diaphragm muscle's contraction and expansion, a positive  $V_{oc}$  signal is generated during inhalation because the volume of the abdomen increases

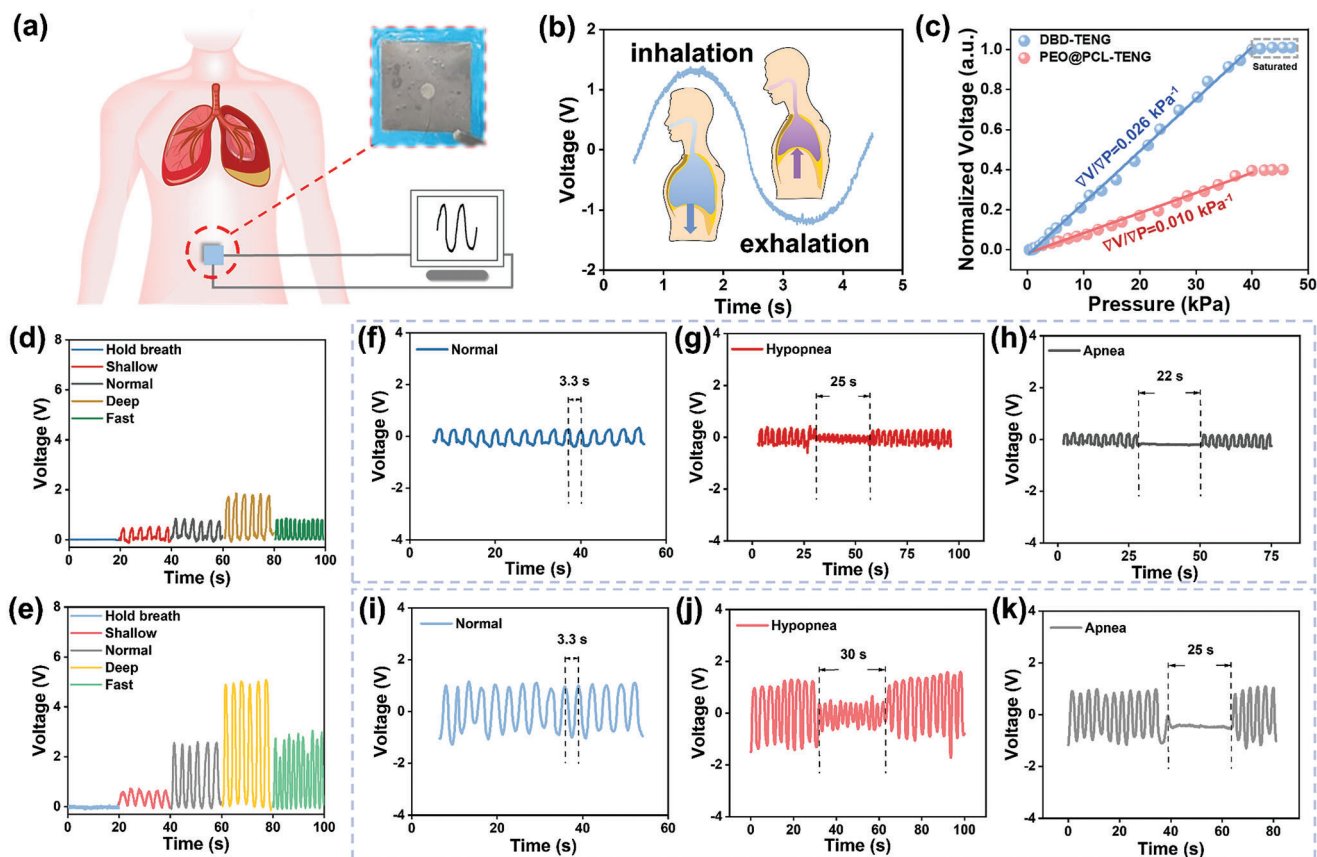


**Figure 6.** Respiratory signal monitoring. a) Schematic diagram of the respiratory monitoring system. b) One complete respiratory waveform containing the process of inhalation and exhalation. c) Normalized output voltage response to a wide range of pressure (0–40 kPa). Real-time voltage signals of different respiratory states, including breath holding, shallow, normal, deep, and fast, monitored from d) PEO@PCL-TENG and e) DBD-TENG. Real-time voltage signals under different sleep respiratory states, including f) normal, g) hypopnea, and h) apnea signals monitored from PEO@PCL-TENG, and i) normal, j) hypopnea, and k) apnea signals monitored from DBD-TENG.

to contact the device. In reverse, a negative  $V_{oc}$  signal is produced during exhalation because the volume of the abdomen decreases to release the device (Figure 6b). The pressure sensitivity of two devices was tested, which is defined as the slope of normalized voltage versus pressure curve, i.e.,

$$S = \frac{d(\nabla V/V)}{dP} \quad (1)$$

Here, the  $\nabla V$  is the relative change in voltage, the  $V$  is the saturation voltage, and the  $P$  is the applied pressure. Within the pressure of 40 kPa, the normalized voltage shows an almost linear relationship, with a sensitivity of  $0.03 \text{ kPa}^{-1}$  for DBD-TENG and  $0.01 \text{ kPa}^{-1}$  for PEO@PCL-TENG (Figure 6c). The enhanced sensitivity of DBD-TENG is attributed to enlarging the polarity difference between PEO and PCL triboelectric materials due to the doping of PPG and EC.

Figure 6d,e depicts the real-time signal diagrams in four breathing patterns of the volunteer monitored by two devices, including breath holding, shallow, deep, and fast, indicating that both devices can distinguish the differences in various breathing states through electrical signals. Under normal circumstances, the breath rate of an adult, on average, is 12 to 20

breaths per minute, corresponding to a respiratory frequency between 0.2 and 0.33 Hz.<sup>[24]</sup> Specifically, there is no fluctuation in the chest and abdomen during the breath-holding state, and neither device produces an output signal. The frequencies in shallow, normal, and deep breathing states are 0.3 Hz, while rapid breathing is 0.55 Hz. The  $V_{oc}$  of shallow, normal, deep, and fast breathing obtained by DBD-TENG are 0.66, 2.51, 4.94, and 2.85 V, respectively. PEO@PCL-TENG yields corresponding values of 0.52, 0.75, 1.78, and 0.84 V. In comparison, DBD-TENG exhibits higher signal outputs and distinct signal differences, facilitating accurate differentiation of various respiratory states.

The DBD-TENG was further developed to monitor different symptoms of obstructive sleep apnea-hypopnea syndrome (OSAHS). Patients with severe OSAHS snore irregularly during sleep, accompanied by repeated respiratory pauses and awakenings. Therefore, wearing sensitive sensors to monitor abnormal respiratory events is crucial for patients. To generate respiratory signals, the volunteer controlled breathing to simulate the hypopnea and apnea of OSAHS patients. Obstructive apnea is a reduction in airflow by more than 90% (even a complete cessation) for at least 10 s. Similarly, hypopnea is a minimum 50% decrease of amplitude in the thoracoabdominal movement for at

least 10 s, followed by a  $\geq 4\%$  fall in oxyhemoglobin saturation.<sup>[25]</sup> The electrical signals of three typical breathing states were measured using PEO@PCL-TENG and DBD-TENG (Figure 6f–k). The signal under normal state (0.3 Hz) is relatively regular (see Figure 6f,i), yet the signal output of DBD-TENG (2.05 V) is significantly higher than that of PEO@PCL-TENG (0.55 V). The occurrence of obstructive respiratory events is accompanied by a reduction or disappearance of amplitude lasting 25 to 30 s (see Figure 6g,h,j,k). During hypopnea, the respiratory signal output of DBD-TENG decreases from 2.30 to 0.87 V, representing an  $\approx 62\%$  reduction in amplitude. Furthermore, the respiratory signal drops by 98% to 0.94 V during apnea. Although the respiratory signal measured by PEO@PCL-TENG decreases to a similar extent as that of DBD-TENG (the hypopnea and apnea states are reduced by 54% and 94%, respectively), the initial signal output is lower (only 0.50 V), leading to the signal difference before and after abnormal respiratory events less obvious. Consequently, due to the higher output performance, DBD-TENG exhibits a more noticeable signal difference in the context of OSAHS, resulting in excellent monitoring sensitivity.

## 2.5. Degradability and Biocompatibility

PEO and PCL are widely recognized biocompatible BPs. To investigate the in vitro degradation performance of PEO/10 wt% PPG and PCL/10 wt% EC composite films, a DBD-TENG device (1.5 cm  $\times$  1.5 cm) was immersed in a constant temperature phosphate buffer saline (37 °C, 1 $\times$  PBS) (Figure 7a) for 300 days. Within the first three months (90 days), the device underwent a long period that appeared stable and unchanged, with only a gradual disappearance of the encapsulation layer's edge. However, the sealed cavity formed by the encapsulation layer still protected the internal structure from the external environment. After 90 days, the encapsulation layer was destroyed, and PBS infiltrated the inner layers. The whole structure degraded together, accelerating the overall degradation rate.

The evaluation of cellular response and the fundamental understanding of in vivo degradation phenomena play a crucial role in designing and developing implantable, biodegradable devices.<sup>[2]</sup> The biocompatibility of composite triboelectric materials, PEO/10 wt% PPG, and PCL/10 wt% EC films was evaluated through CCK-8 assay and cell viability/cytotoxicity testing experiments (Figure 7b,c; Figures S14 and S15, Supporting Information). The results indicated that neither composite materials affect the activity of NIH3T3 cells or cell proliferation, which suggests that both PEO/10 wt% PPG and PCL/10 wt% EC composite materials exhibit excellent biocompatibility. To comprehend the in vivo degradation behavior of DBD-TENG, we implanted the device (1.5 cm  $\times$  1.5 cm) in the subdermal dorsal region of a Sprague-Dawley (SD) rat (Figure 7d). The low Young's modulus of the flexible device ( $61.29 \pm 2.20$  MPa) enabled it to conform closely to the skin tissue without mechanical mismatch problems (Figure S13, Supporting Information). In the initial stage, the device rapidly degraded from the edge. The edge of the encapsulation layer completely disappeared after 7 days of implantation, which caused the exposure of the internal structure to the body fluid and accelerated degradation. After 30 days, the entire device exhibited a noticeable reduction in

volume with the serrated edge. By 90 days, further degradation was observed. The degradation rate of the device in vivo is obviously faster than in vitro, presumably due to the joint effect of the body fluid and lipase that accelerates degradation (Figure 7g). The DBD-TENG was implanted into the chest of the rat. As the implanted device was driven by a slight external force and respiratory movement of the resting-state rat, respectively, the  $V_{oc}$  outputs of  $\approx 1.10$  V and  $\approx 50$  mV (Figure 7e,f) were obtained, indicating the ability to harvest mechanical energy in vivo of DBD-TENG.

## 3. Conclusion

In conclusion, the triboelectric polarities of the tribopositive PEO and tribonegative PCL materials can be further improved by doping chosen biocompatible molecules. We thoroughly compared the triboelectric polarity of the composite films and corresponding doping molecules and researched related mechanisms. The DBD-TENG based on PEO/PPG and PCL/EC composite films demonstrated an  $\approx 2.5$  times improvement in the output performance ( $V_{oc}$ ,  $I_{sc}$ , and  $Q_{sc}$ ), and its resolution in abnormal respiratory signal monitoring was significantly enhanced. This work not only provides theoretical guidance for the selection of biocompatible triboelectric molecules but also conducts in-depth research in molecular-level triboelectric mechanisms.

## 4. Experimental Section

**BTPs, Doping Molecules, and Solvents:** Polyethylene oxide (PEO,  $M_v \approx 100000$ ), polycaprolactone (PCL,  $M_v \approx 60000$ ), and trichloromethane (TCM, AR,  $\geq 99.0\%$ ) were purchased from Sigma–Aldrich. Hydroxypropyl cellulose (HPC,  $M_w \approx 100000$ ), polylactic acid (PLA), poly(trimethylene carbonate) (PTMC,  $M_v \approx 50000$ ), spermidine (SPD, 99%), citric acid (CA, AR), sodium citrate (SC), oleic acid (OA, 85%), ethyl cellulose (EC,  $M_r \approx 448.47$ ), and 1,1,1,3,3,3-Hexafluoro-2-propanol (HFIP, 99.5%) were purchased from Aladdin. 1,1-Dimethylguanidine (DMG,  $\geq 95\%$ ), glycerol (99.5%), reduced graphene oxide (rGO, SE1233,  $< 0.10$  g cm $^{-3}$ , 5–10  $\mu$ m,  $\geq 97\%$ ), and MXene ( $Ti_3C_2T_x$ , 2–5  $\mu$ m, 3.43 g cm $^{-3}$ , 99 wt%) multilayer nanoflake were purchased from Macklin. D-mannitol (99.9+%), poly(ethylene glycol) (PEG,  $M_n \approx 400$ ), poly(propylene glycol) (PPG,  $M_n \approx 400$ ), perfluorodecalin (PFD, 98%), sodium chloride (NaCl, AR, 99.5%, 2.17 g cm $^{-3}$ ), sodium fluoride (NaF, 99%, 2.56 g cm $^{-3}$ ), and sucralose (98%) were purchased from Innochem.

**The Preparation of Films:** The films were prepared by a simple one-step dissolution method. The pure films (PEO, PCL, HPC, and PLA) and encapsulation layers (PTMC) were made by dissolving 0.50 g of corresponding solid powder into  $\approx 20$  mL solvent, respectively. The composite films were prepared by adding polymer matrix (PEO, PCL, HPC, and PLA) powder and doping molecules (SPD, DMG, CA, SC, glycerol, D-mannitol, PEG, and PPG were doped in tribopositive films, PFD, OA, NaCl, NaF, rGO, MXene, sucralose, and EC were doped in tribonegative films) into  $\approx 20$  mL solvent. Stir evenly to form a homogeneous solution. After removing the bubbles by standing for a while, the resulting solutions were poured into Petri dishes of the same specification (diameter = 6.6 cm). Finally, the thin films were obtained after drying at 40 °C for 48 h. All films' solvent and doping content are listed in Table S1 (Supporting Information) in detail.

**The Fabrication of BD-TENG:** The as-prepared films were tailored into a square shape with a dimension of 2.0 cm  $\times$  2.0 cm. Then, an electrode layer was deposited by the sputtering of magnesium (Mg) (General Research Institute of Nonferrous Metals, Beijing, China) on the rough side. A Mg wire was connected to the electrode. The two triboelectric layers were fixed together with a spacer of 1 mm set between them. The PTMC films

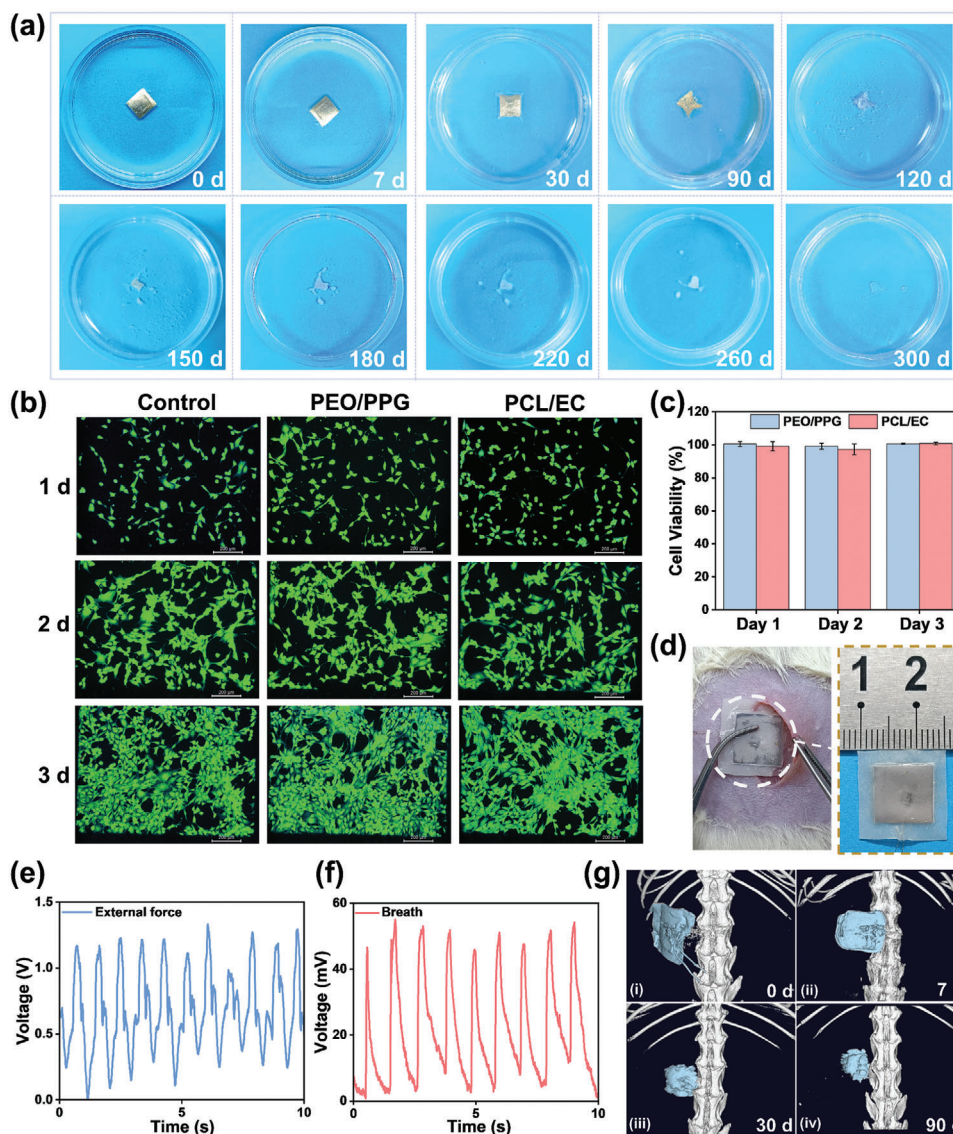


**Figure 7.** Biodegradability and biocompatibility. a) Degradation performance in vitro of DBD-TENG. b) Fluorescence images of stained NIH3T3 cells and sterilization results of PEO/10 wt% PPG and PCL/10 wt% EC films. c) Viability of NIH3T3 cells after being cultured for 3 days. All data are presented as the mean  $\pm$  standard error of mean ( $n = 4$  independent samples). d) Images of the implanted DBD-TENG and the demonstration for location in the chest region of an SD rat. The  $V_{oc}$  outputs of the implanted DBD-TENG driven by e) a slight external force and f) respiratory movement of the resting-state rat in vivo. g) Micro-CT images of the implanted DBD-TENG (blue area) after 90 days of implantation demonstrate the degree of degradation of DBD-TENG in vivo.

of proper size were employed as the encapsulation layers of the device through heat sealing.

**Triboelectric Properties:** To obtain more accurate results, the doping content was kept, preparation process, and testing conditions of triboelectric films as consistent as possible, including humidity ( $16\% \pm 2\%$ ), temperature ( $22 \pm 1^\circ\text{C}$ ), film size of  $2.0\text{ cm} \times 2.0\text{ cm}$ , and film thickness of  $110 \pm 20\ \mu\text{m}$ . Four BTPs and tribopositive films were in contact with PTFE, while tribonegative films were with PEO. A linear motor (LinMot E1100) was used to provide periodic contact separation motion for the electrical measurement of triboelectric pairs and the contact-separation (CS) BD-TENG device. The open circuit voltage ( $V_{oc}$ ), short circuit current ( $I_{sc}$ ), and transfer charge ( $Q_{sc}$ ) of triboelectric pairs were measured through an electrometer (Keithley 6517B) and recorded by an oscilloscope (Teledyne LeCroy HD 4096).

**Respiratory Signal Monitoring:** A device of  $2.0\text{ cm} \times 2.0\text{ cm}$  was fixed above the navel of the volunteer's abdomen by a medical bandage. The Mg wires of the device were connected with an electrometer (Keithley 6517B), and respiratory signals were recorded by an oscilloscope (Teledyne LeCroy HD 4096).

**Bio-Test:** Rat embryonic fibroblasts (NIH3T3) were derived from the Cell Bank of the Chinese Academy of Sciences in Beijing, China. NIH3T3 cells were cultured in a DMEM high glucose medium containing 10% fetal bovine serum (FBS) and 1% penicillin/streptomycin at  $37^\circ\text{C}$  and 5%  $\text{CO}_2$  for the cell viability testing experiment. 10% FBS was replaced by 3% while other conditions were kept the same for the cell cytotoxicity testing experiment. The material extraction solution was obtained by soaking 100 mg PEO/PPG film and PCL/EC film in 1 mL medium for three days in the viability testing experiment and five days in the cytotoxicity testing experiment,

respectively.  $10^3$  NIH3T3 cells were implanted in 96-well plates. CCK-8 kit and cell viability/cytotoxicity detection kit were used to detect cell activity after 24, 48, and 72 h with the material extract in the viability testing experiment and five days in the cytotoxicity testing experiment, respectively. The in vitro degradability of DBD-TENG was performed in 15 mL  $1\times$  PBS solution in a microbial incubator at 37 °C. The photographs of the device were obtained by a camera periodically during the degradation. The in vivo degradability of the device was observed in the subdermal dorsal region of a male Sprague-Dawley (SD) rat. The procedure strictly followed the “Beijing Administration Rule of Laboratory Animals” and the national standards of “Laboratory Animal Requirements of Environment and Housing Facilities (GB14925-2001)”. All the animal experiments were under ethical approval from the Committee on Ethics of the Beijing Institute of Nanoenergy and Nanosystems. The biodegradation process was tracked by micro-CT for 90 days. An external force by a slight finger tap on the skin of the implanted region and respiratory movement of the diaphragm drive the implanted DBD-TENG to produce  $V_{oc}$  outputs. The output property of the device in vivo was evaluated. The as-generated output signals were measured by connecting the Mg wires to the electrodes of the oscilloscope.

**Other Characterizations:** Fourier transform infrared (FTIR) spectra were obtained using a VERTEX80v spectrometer (Bruker, Karlsruhe, Germany). The scanning electron microscopy (SEM) image was collected using a Hitachi field emission scanning electron microscope (SU 8020). The tensile test of films and the device were performed on an ESM301/Mark-10 system (Mark-10 Company, New York, NY, USA) with a tensile rate of 30 mm  $\text{min}^{-1}$ . The size of the tensile test samples was 20 mm  $\times$  5 mm.

## Supporting Information

Supporting Information is available from the Wiley Online Library or from the author.

## Acknowledgements

This work was supported by the National Natural Science Foundation of China (T2125003, 52203325), National Key Research and Development Program of China (2022YFB3804703, 2022YFB3804704, and 2021YFB3200303), Beijing Natural Science Foundation (L212010), and the Fundamental Research Funds for the Central Universities.

## Conflict of Interest

The authors declare no conflict of interest.

## Data Availability Statement

The data that support the findings of this study are available from the corresponding author upon reasonable request.

## Keywords

biocompatibility, molecular doping, output performance, triboelectric nanogenerators, triboelectric polarity

Received: January 6, 2024  
Revised: February 29, 2024  
Published online:

[1] a) T. H. Cheng, J. J. Shao, Z. L. Wang, *Nat. Rev. Methods Primers* **2023**, 3, 39; b) D. Choi, Y. Lee, Z. H. Lin, S. Cho, M. Kim, C. K. Ao, S. Soh, C.

- Sohn, C. K. Jeong, J. Lee, M. Lee, S. Lee, J. Ryu, P. Parashar, Y. Cho, J. Ahn, I. D. Kim, F. Jiang, P. S. Lee, G. Khandelwal, S. J. Kim, H. S. Kim, H. C. Song, M. Kim, J. Nah, W. Kim, H. G. Menge, Y. T. Park, W. Xu, J. Hao, et al., *ACS Nano* **2023**, 17, 11087.
- [2] Q. Zheng, Y. Zou, Y. Zhang, Z. Liu, B. Shi, X. Wang, Y. Jin, H. Ouyang, Z. Li, Z. L. Wang, *Sci. Adv.* **2016**, 2, e1501478.
- [3] S. Y. Chao, H. Ouyang, D. J. Jiang, Y. B. Fan, Z. Li, *Ecomat* **2021**, 3, e12072.
- [4] D. Liu, L. Zhou, S. Cui, Y. Gao, S. Li, Z. Zhao, Z. Yi, H. Zou, Y. Fan, J. Wang, Z. L. Wang, *Nat. Commun.* **2022**, 13, 6019.
- [5] H. Meng, Q. Yu, Z. Liu, Y. Gai, J. Xue, Y. Bai, X. Qu, P. Tan, D. Luo, W. Huang, K. Nie, W. Bai, Z. Hou, R. Tang, H. Xu, Y. Zhang, Q. Cai, X. Yang, Z. L. Wang, Z. Li, *Matter* **2023**, 6, 4274.
- [6] a) P. Ding, J. K. Chen, U. Farooq, P. F. Zhao, N. Soin, L. Y. Yu, H. Jin, X. Z. Wang, S. R. Dong, J. K. Luo, *Nano Energy* **2018**, 46, 63; b) S. Y. Li, Y. Fan, H. Q. Chen, J. H. Nie, Y. X. Liang, X. L. Tao, J. Zhang, X. Y. Chen, E. G. Fu, Z. L. Wang, *Energy Environ. Sci.* **2020**, 13, 896; c) J. Zhang, Y. Zheng, L. Xu, D. Wang, *Nano Energy* **2020**, 69, 104435; d) H. Feng, Y. Bai, L. Qiao, Z. Li, E. Wang, S. Chao, X. Qu, Y. Cao, Z. Liu, X. Han, R. Luo, Y. Shan, Z. Li, *Small* **2021**, 17, 2101430; e) Q. Zhang, C. Huang, Y. Zhang, S. Liu, D. Zhang, P. Li, F. Wang, D. Wang, Y.-Y. Zhang, *Chem. Eng. J.* **2024**, 482, 148854; f) C. Huang, S. Zhang, S. Liu, Q. Zhang, Y.-Y. Zhang, L. Mi, *Chem. - Eur. J.* **2023**, 29, 202300528; g) G. Lu, C. Huang, M. Qiu, Q. Zhang, S. Cui, L. Zhang, Y.-Y. Zhang, L. Mi, *Inorg. Chem.* **2022**, 61, 12736; h) C. Huang, G. Lu, Y. Zhang, K. Zhu, S. Cui, W. Chen, Z. Wu, M. Qiu, L. Mi, *Inorg. Chem.* **2021**, 60, 550; i) P. Zhao, G. Bhattacharya, S. J. Fishlock, J. G. M. Guy, A. Kumar, C. Tsonos, Z. Yu, S. Raj, J. A. McLaughlin, J. Luo, N. Soin, *Nano Energy* **2020**, 75, 104958.
- [7] a) A. Haleem, Z. Haider, R. U. S. Ahmad, U. P. Claver, A. F. Shah, G. Zhao, W. D. He, *Int. J. Energy Res.* **2020**, 44, 8442; b) C. Wu, T. W. Kim, H. Y. Choi, *Nano Energy* **2017**, 32, 542; c) Q. Zhang, C. Huang, D. Zhang, Y. Zhang, F. Wang, N. Liu, D. Wang, Y.-Y. Zhang, L. Mi, *ACS Mater. Lett.* **2023**, 5, 2700.
- [8] Z. Zhang, W. Z. Gong, Z. Q. Bai, D. F. Wang, Y. Y. Xu, Z. T. Li, J. S. Guo, L. S. Turng, *ACS Nano* **2019**, 13, 12787.
- [9] Y. H. Wu, Y. Luo, J. K. Qu, W. A. Daoud, T. Qi, *ACS Appl. Mater. Interfaces* **2020**, 12, 55444.
- [10] Y. Lyu, Y. Wang, *Nano Energy* **2022**, 103, 107811.
- [11] S. Y. Li, J. H. Nie, Y. X. Shi, X. L. Tao, F. Wang, J. W. Tian, S. Q. Lin, X. Y. Chen, Z. L. Wang, *Adv. Mater.* **2020**, 32, 2001307.
- [12] a) S. Zellnitz, J. T. Pinto, M. Brunsteiner, H. Schroettner, J. Khinast, A. Paudel, *Pharm. Res.* **2019**, 36, 80; b) C. X. Gao, W. S. Tong, S. L. Liu, X. M. Wang, Y. H. Zhang, *Nano Energy* **2023**, 117, 108876.
- [13] S. H. Shin, Y. E. Bae, H. K. Moon, J. Kim, S. H. Choi, Y. Kim, H. J. Yoon, M. H. Lee, J. Nah, *ACS Nano* **2017**, 11, 6131.
- [14] a) Q. N. Yu, S. C. Jin, S. C. Wang, H. N. Xiao, Y. T. Zhao, *Chem. Eng. J.* **2023**, 452, 139252; b) A. Domínguez-Bajo, A. González-Mayorga, C. R. Guerrero, F. J. Palomares, R. García, E. López-Dolado, M. C. Serrano, *Biomaterials* **2019**, 192, 461; c) Y. Liu, H. Zhou, W. X. Zhou, S. Meng, C. Qi, Z. Liu, T. T. Kong, *Adv. Energy Mater.* **2021**, 11, 2101329.
- [15] A. Chaiwat, E. Chunhacheevachaloke, P. Kidkhunthod, P. Pakawanit, O. A.-O. Ajcharanukul, *J. Dent. Res.* **2023**, 102, 402.
- [16] P. Hafezifefat, J. K. Lindstrom, R. C. Brown, L. Qi, *Green Chem.* **2020**, 22, 6567.
- [17] L. K. Wang, H. C. Xu, F. C. Huang, X. M. Tao, Y. F. Ouyang, Y. L. Zhou, X. M. Mo, *Nanomaterials* **2022**, 12, 3217.
- [18] K. P. McKenna, A. L. Shluger, *Nat. Mater.* **2008**, 7, 859.
- [19] a) S. M. Niu, S. H. Wang, L. Lin, Y. Liu, Y. S. Zhou, Y. F. Hu, Z. L. Wang, *Energy Environ. Sci.* **2013**, 6, 3576; b) Y. K. Liu, W. L. Liu, Z. Wang, W. C. He, Q. Tang, Y. Xi, X. Wang, H. Y. Guo, C. G. Hu, *Nat. Commun.* **2020**, 11, 1599.
- [20] a) S. Ippili, V. Jella, A. M. Thomas, C. Yoon, J. S. Jung, S. G. Yoon, J. Mater. Chem. A **2021**, 9, 15993; b) Z. H. Peng, X. Xiao, J. X. Song, A.

- Libanori, C. Lee, K. D. Chen, Y. Gao, Y. S. Fang, J. Wang, Z. K. Wang, J. Chen, M. K. H. Leung, *ACS Nano* **2022**, *16*, 20251.
- [21] a) S. Fleming, M. Thompson, R. Stevens, C. Heneghan, A. Plüddemann, I. Maconochie, L. Tarassenko, D. Mant, *Lancet* **2011**, *377*, 1011; b) S. C. Gandevia, D. K. McKenzie, *Med. J. Aust.* **2008**, *189*, 531.
- [22] H. W. Liu, J. Dong, H. Y. Zhou, X. D. Yang, C. Y. Xu, Y. Q. Yao, G. D. Zhou, S. Zhang, Q. L. Song, *ACS Appl. Electron. Mater.* **2021**, *3*, 4162.
- [23] X. Peng, K. Dong, C. A. Ning, R. W. Cheng, J. Yi, Y. H. Zhang, F. F. Sheng, Z. Y. Wu, Z. L. Wang, *Adv. Funct. Mater.* **2021**, *31*, 2103559.
- [24] P. B. Lovett, J. M. Buchwald, K. Stürmann, P. Bijur, *Ann. Emerg. Med.* **2005**, *45*, 68.
- [25] a) C. Pérez-Rico, E. Gutiérrez-Díaz, E. Mencía-Gutiérrez, M. Díaz-de-Atauri, R. Blanco, *Graef. Arch. Clin. Exp.* **2014**, *252*, 1345; b) F. Campos-Rodriguez, M. A. Martínez-García, N. Reyes-Nuñez, M. J. Selma-Ferrer, N. M. Punjabi, R. Farre, *Sleep Med.* **2016**, *27*, 54.